Original Research

Physico-Chemical Study of the Anti-Diabetic Drug of [BzN-EJJ-amide] for Treatment Type2 Diabetes Using CNT Sensor by Drug Delivery Method

Fatemeh Mollaamin [1, *], Majid Monajjemi [2], Ahmad R. Alsayed [3]

1. Department of Biomedical Engineering, Faculty of Engineering and Architecture, Kastamonu University, Kastamonu, Turkey; E-Mails: fmollaamin@kastamou.edu.tr; smollaamin@gmail.com
2. Department of Chemical Engineering, Central Tehran Branch, Islamic Azad University, Tehran, Iran; E-Mail: maj.monajjemi@iauctb.ac.ir
3. Department of Clinical Pharmacy and Therapeutics, Faculty of Pharmacy, Applied Science Private University, Amman, Jordan; E-Mails: a_alsayed@asu.edu.jo; a.alsayed.phd@gmail.com

* **Correspondence:** Fatemeh Mollaamin; E-Mails: fmollaamin@kastamou.edu.tr; smollaamin@gmail.com

Academic Editor: Lunawati L Bennett

Abstract

The potential and selective inhibitors of protein tyrosine phosphatase 1B (PTP1B) are therapeutically useful in treating type 2 diabetes. N-Benzoyl-L-glutamyl-[4-phosphono(difluoromethyl)]-L-phenylalanine-[4-phosphono(difluoro-methyl)]-L-phenylalanineamide (BzN-EJJ-amide) (BGD) which is the ligand of 1LQF protein code extracted from protein data bank (PDB) is an inhibitor of PTP-1B that indicates selectivity over several protein tyrosine phosphatases. In this research, the interaction between the anti-diabetic drug of BzN-EJJ-amide and armchair single-walled carbon nanotube (SWCNT) has been investigated based on Density Functional Theory (DFT) theory to design, improve and expand carbon nanotube drug carriers as the applied sensors in drug delivery systems. Therefore, physico-chemical properties of optimized geometry, quantum molecular descriptors,

topological parameters, and frontier molecular orbitals of different drug arrangements on CNT at the highest equilibrium at CAM-B3LYP/6-311+G (2d,p) level of theory have been explored. The results of Nuclear Magnetic resonance (NMR), Natural Bond Orbital (NBO), Infrared (IR), and charge distributions have indicated that BzN-EJJ-amide → (5, 5) armchair SWCNT complex presents the position of active sites of labeled N, O, P, and F atoms in this linkage, which transfer the charge of electrons in polar bisphosphonate agent of BzN-EJJ-amide toward (5, 5) armchair SWCNT sensor. Evaluation of the results obtained from the electrostatic potential (ESP) map, Frontier orbitals of HOMO, LUMO, and UV-VIS spectroscopy analysis have exhibited that the direction of electron movement is generally from drug molecule to carbon nanotube as the sensor for BzN-EJJ-amide anti-diabetes drug.

## 1. Introduction

Type 2 diabetes mellitus is an advanced illness described by deficiencies in insulin secretion and augmented insulin persistence directed to abnormal glucose metabolism and relevant metabolic disorders. Although the aetiologies of type 1 and type 2 diabetes vary enormously, both indicate hyperglycaemic states, and both exhibit common macrovascular such as cerebrovascular, coronary heart, and peripheral vascular disease and microvascular complications like neuropathy, nephropathy, and retinopathy [1-5].

Phosphoeleganin is applied to stop both enzymes, acting respectively as a pure non-competitive inhibitor of PTP1B and a mixed-type inhibitor of AR. Furthermore, in silico docking analyses, the interaction mode of phosphoeleganin with both enzymes was estimated. The inhibitory mechanism of protein tyrosine phosphatase 1B (PTP1B) and aldose reductase (AR) enzymes containing analysis of the insulin signaling pathway of phosphoeleganin was investigated [6].

Inhibitors of PTP-1B can be effective in the remedy of type 2 diabetes disease. Considering the large number of phosphatases in the cell, inhibitors against PTP-1B should be selective and potent. Some research has investigated the crystal compounds of PTP-1B in complex with BzN-EJJ-amide at 2.5 A resolution. The results exhibited a high inhibitory ability through interactions of several of its chemical groups with particular protein residues. An interaction between BzN-EJJ-amide and Asp48 is of particular significance, as the substitution of Asp48 to alanine resulted in a 100-fold loss in potency (Scheme 1) [7].
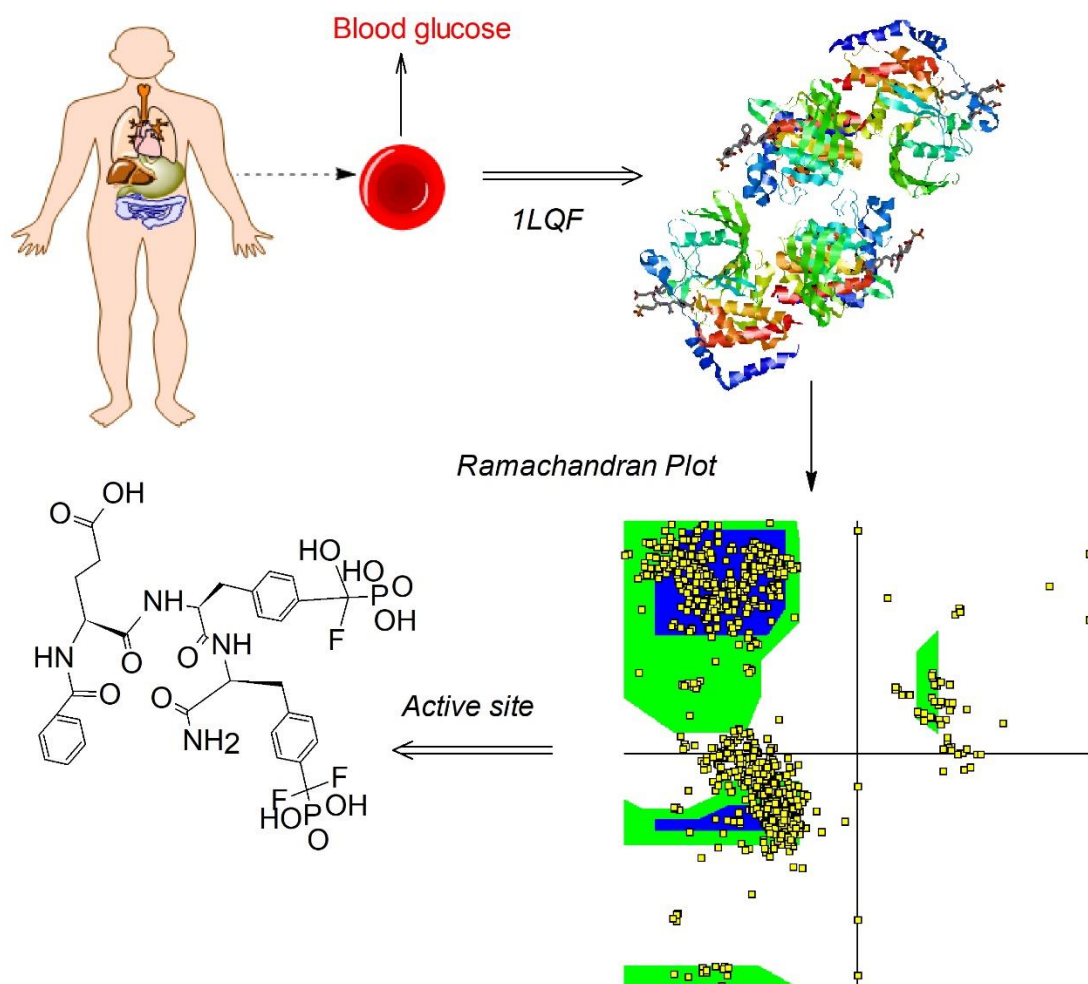
Scheme 1 Bisphosphonate agent of BzN-EJJ-amide extracted from protein 1LQF accompanying the Ramachandran plot.

The structure of PTP-1B in a complex with a peptide inhibitor reveals an alternative binding mode for bisphosphonates. The crystal structure also revealed an unexpected binding orientation for a bisphosphonate inhibitor on PTP-1B, where the second difluorophosphonomethyl phenylalanine moiety is linked to near Arg47 rather than in the formerly distinguished second aryl phosphate site indicated by Arg24 and Arg254. The data recommends that potent and selective PTP-1B inhibitors may be designed by targeting the region containing Arg47 and Asp48f (Scheme 1) [8, 9].

Nanomedication contains a broad range of therapeutic usages, from nanoparticle drug delivery systems consisting of carbon nanotubes or layered double hydroxides as biosensors and imaging and implantable devices diagnostics [10-18]. Carbon nanotubes are considerable in the nanomedication industry because of their unique attributes, such as thermal, mechanical, electromagnetical, and other physical and chemical properties [19-21]. CNTs represent their ability to carry over remedial agents consisting of medications, macromolecules of proteins, or antibodies through attaching and releasing the drug in the body cell [22-29]. Single-walled carbon nanotubes are produced by wrapping a single layer of graphite cylinder; multi-walled carbon nanotubes are multiple concentric cylindrical shells of graphite layers [30-41].

The structures of Non-N-containing bisphosphonates such as etidronate, tiludronate, and clodronate are studied as the first generation of bisphosphonates that are plain molecules

consisting of single atoms or alkyl groups in side chains of R1 and R2 side chains having a weak inhibition effect on bone resorption [42-50]. These days, the third generation of bisphosphonates containing N-heterocyclic bisphosphonates, such as zoledronate and risedronate, have illustrated the most potent antiresorptive specifications [51-56]. In this research, the interaction between the anti-diabetic drug of BzN-EJJ-amide and SWCNT has been investigated based on the DFT method to evaluate the potential of SWCNT as the sensitive sensors in drug delivery systems through physicochemical analysis.

2. Materials and Methods

In this research, it has been described the electronic structure of adsorbed (5, 5) armchair SWCNT by bisphosphonate agent of BzN-EJJ-amide extracted from protein 1LQF for measuring physicochemical properties (Scheme 2).
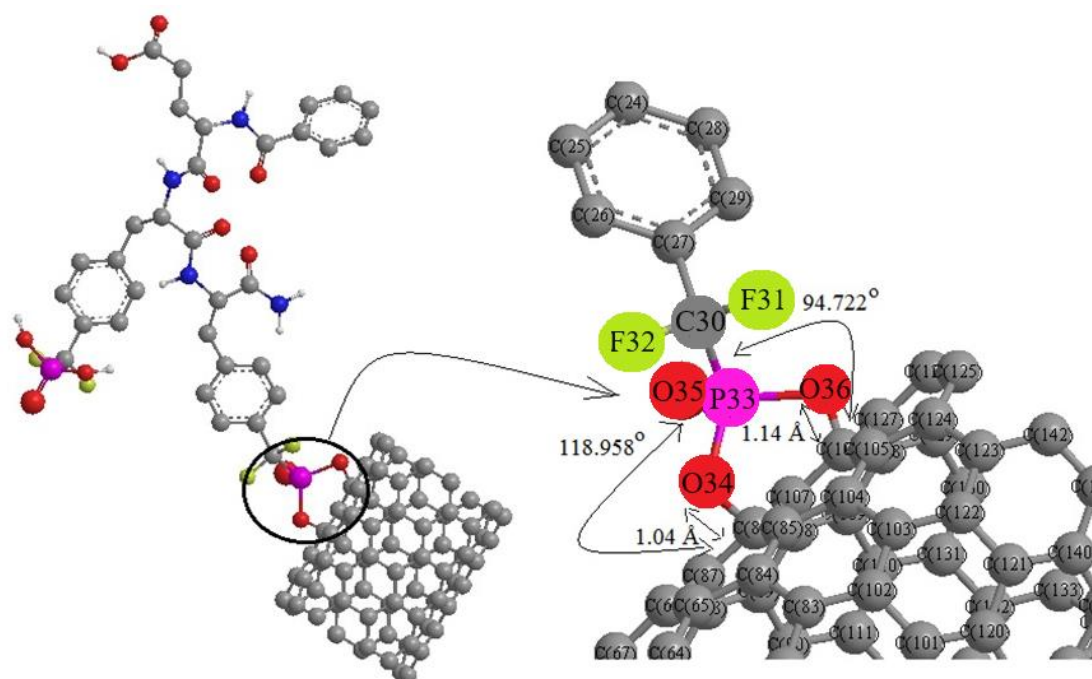
Scheme 2 Adsorption of active site molecule derived of (BzN-EJJ-amide) extracted from 1LQF PDB on the (5, 5) armchair SWCNT.

The approximations of Hohenberg, Kohn, and Sham use the density functional theory (DFT) for exploring the specification of materials [57] and for foretelling chemical systems and perceiving their similarities and differences compared to other computational approaches [58-60]. Then, a new hybrid exchange-correlation functional named CAM–B3LYP is proposed. It combines the hybrid qualities of B3LYP and the long-range correction. We demonstrate that CAM–B3LYP yields atomization energies of similar quality to those from B3LYP while also performing well for charge transfer excitations in our model, which B3LYP underestimates enormously [58-60].

The Onsager model was employed in this research, accompanying the solvent dielectric effect. A cavity generates this model to keep out the solvent and contain frontiers as part of the solute charge distribution [61-68].

The NQR is a straight frame of the interaction of the quadrupole moment with the local electric field gradient (EFG) generated by its ambiance's electronic structure:

$$V(r) = V(0) + \left[\left(\frac{\partial V}{\partial x_i}\right)\Big|_0 \cdot x_i\right] + \frac{1}{2}\left[\left(\frac{\partial^2 V}{\partial x_i x_j}\right)\Big|_0 \cdot x_i x_j\right] + \cdots \tag{1}$$

After simplification of the equation, there are only the second derivatives related to the same variable for the potential energy [69, 70]:

$$U = -\frac{1}{2}\int_{\mathcal{D}} d^3 r \rho_r \left[\left(\frac{\partial^2 V}{\partial x_i^2}\right)\Big|_0 \cdot x_i^2\right] = -\frac{1}{2}\int_{\mathcal{D}} d^3 r \rho_r \left[\left(\frac{\partial E_i}{\partial x_i}\right)\Big|_0 \cdot x_i^2\right] =$$
$$-\frac{1}{2}\left(\frac{\partial E_i}{\partial x_i}\right)\Big|_0 \cdot \int_{\mathcal{D}} d^3 r [\rho(r) \cdot x_i^2] \tag{2}$$

Two parameters must be obtained from NQR experiments; the quadrupole coupling constant, χ, and asymmetry parameter of the EFG tensor η:

$$\chi = \frac{e^2 Q q_{zz}}{h} \tag{3}$$

$$\eta = \frac{q_{xx} - q_{yy}}{q_{zz}} \tag{4}$$

where q_{ii} are components of the EFG tensor at the quadrupole nucleus determined in the EFG principal axes system, Q is the nuclear quadrupole moment, e is the proton charge, and h is the Planck's constant [71]. The graph of NQR characteristics for BzN-EJJ-amide → (5, 5) armchair SWCNT complex has the most fluctuation in the region of two phosphorus of PO_3 groups (Scheme 2).

The electric potential ($J \cdot C^{-1}$) is a continuous function in space produced by an idealized point charge that has $1/r$ potential: $V_E = \frac{1}{4\pi\varepsilon_0}\frac{Q}{r}$, where Q (measured in coulombs) is the point charge, r is the distance from the charge and ε_0 is the permittivity of a vacuum. Since the electric potential for a system of point charges is equal to the sum of the point charges' potentials, the calculations are done based on the summation of potential fields, which is scalar instead of the summation of the electric fields, which is vector and much more difficult than potential field. So, $V_E(r) = \frac{1}{4\pi\varepsilon_0}\sum_i \frac{q_i}{|r-r_i|}$, where r is the point at which the potential is measured, r_i is a point at which the charge is $\neq 0$, and q_i is the charge at the point r_i. Finally, the potential of a continuous charge distribution $\rho(r)$ appears: $V_E(r) = \frac{1}{4\pi\varepsilon_0}\int_R \frac{\rho(r')}{|r-r'|}d^3 r'$, where R is a region including all the points at which the charge density is $\neq 0$, r' is a point inside R, and $\rho(r')$ is the charge density at the point r' [72]. The ESP $\varphi(r)$ at position r due to a charge Q_j at position r_j is explained as:

$$\varphi(r) = \frac{Q_j}{4\pi\varepsilon_{0|r-r_j|}} \tag{5}$$

where ε_0 is the permittivity of free space. A charge density $\rho_{tot}(r)$ is illustrated in units of elementary charge per volume as the difference between proton and electron densities [73].

The ESP can also be expressed as an inverse Fourier transform involving the structure factors of the total charge density:

$$\varphi_{stat}(r) = \frac{1}{\pi V_{UC}}\left[\varphi_0 + \sum_{H}^{|H|_{max}} \frac{F_{tot}(H)}{|H|^2}\exp(-2\pi iH.r)\right] \qquad (6)$$

The total charge density of a periodic structure can then be expressed as the inverse Fourier transform of its structure factors, where the latter are defined on the nodes H of the reciprocal lattice and V_{UC} is the volume of the unit cell, and the term $H = 0$ is excluded from the summation. The macroscopic contribution φ_0 to the ESP is [74]:

$$\varphi_0 = -\frac{2\pi}{3}\sum_{\alpha=1}^{3}\sum_{\beta=1}^{3} g_{\alpha\beta}Q_{\alpha\beta} \qquad (7)$$

$g_{\alpha\beta}$ being the metric tensor and $Q_{\alpha\beta}$ The quadrupolar tensor obtained by the summation rules [74].

Owing to the additional factor of $\frac{1}{|H|^2}$, ESP is expected to have a more rapid convergence. This observation directs us to the hypothesis that equation (6) for $\varphi_{stat}(r)$ will change quickly if $F_{tot}(H)$ is substituted by the structure factor of the dynamic charge density.

$$F_{tot}^{dyn}(H) = \sum_{j=1}^{N_{vc}}[Z_j - f_j(H)]T^j(H)\exp(2\pi iH.r_j) \qquad (8)$$

where $T^j(H)$ is the Debye–Waller factor of atom j. Therefore, it shows the logical choice for dynamic ESPs based on structure models [74].

3. Results and Discussion

3.1 Charge Distribution & NMR Analysis

The NMR data of isotropic (σ_{iso}) and anisotropic shielding tensor (σ_{aniso}) for BzN-EJJ-amide adsorbed on the (5, 5) armchair SWCNT has been estimated (Table 1). The calculations were accomplished based on CAM-B3LYP/6-311+G (2d,p) level of theory using the Gaussian 16 revision C.01 program [75] and are reported in Table 1.

Table 1 SCF GIAO magnetic shielding tensor for BzN-EJJ-amide.

Atom type	Atomic charge	σ_{iso}	σ_{aniso}	Electric potential
P1	1.2338	610.2649	254.6516	53.1218
O2	-0.5892	355.5439	154.0376	-22.3102
O3	-0.2477	162.1295	85.5850	-22.0429
O4	-0.2491	410.1194	78.5889	-22.0374
F6	-0.1578	468.1859	60.3943	-26.1399
F7	-0.127	60.3943	59.1620	-26.1408
O17	-0.2882	-81.5346	842.8826	-22.0677
N18	-0.182	250.5042	93.4209	-18.0714
N22	-0.0263	256.9351	96.1496	-18.1144
O23	-0.3013	-79.6592	835.5614	-22.1040

F31	-0.1587	463.1448	61.4132	-26.1763
F32	-0.1543	459.9514	57.1339	-26.1688
P33	1.2417	601.4013	234.5514	-53.1392
O34	-0.2479	416.0570	85.1314	-22.0544
O35	-0.6183	359.4198	138.0327	-22.3364
O36	-0.2532	394.5909	79.1138	-22.0700
N37	-0.1704	251.3748	90.0816	-18.0585
O39	-0.2993	-71.5692	831.6598	-22.0684
O44	-0.0936	263.9460	104.1935	-21.9779
O45	-0.2774	-111.5997	837.7114	-22.0415
N46	-0.1744	258.6383	91.1142	-18.0820
O48	-0.2895	-110.3208	917.7161	-22.0921

In the aqueous medium, the agent of BzN-EJJ-amide attached to (5, 5) armchair SWCNT has exhibited the fluctuation manner for various atoms of nitrogen, phosphorus, oxygen, and fluorine in the active zones of this compound through the NMR chemical shielding tensor (Figure 1).
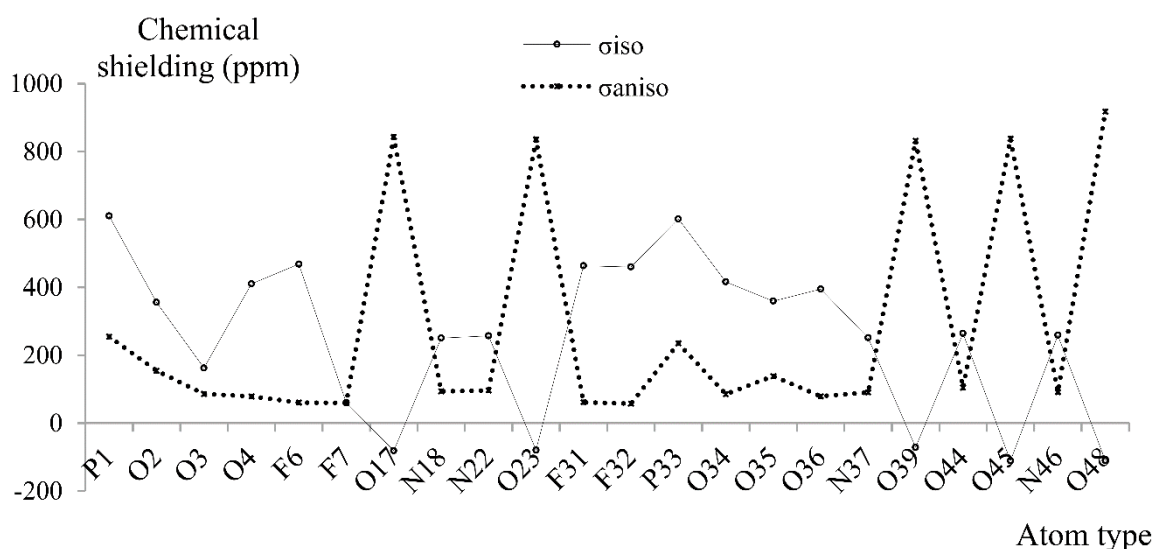

Figure 1 The chemical shielding of ^{13}C-NMR: isotropic (σ_{iso}) and anisotropic (σ_{aniso}) calculated for BzN-EJJ-amide using SCF GIAO method due to CAM-B3LYP method.

The chemical shielding tensors have been resulted by the theoretical computations in the principal axes system to guess the isotropic chemical-shielding (CSI), ($\sigma_{33} + \sigma_{22} + \sigma_{11}$)/3, and anisotropic chemical-shielding (CSA), $\sigma_{33} - (\sigma_{22} + \sigma_{11})$/2 [75]. Furthermore, the Onsager model has been used to calculate NMR parameters and chemical shielding of H, C, N, O, P, and F elements in BzN-EJJ-amide (Figure 2).
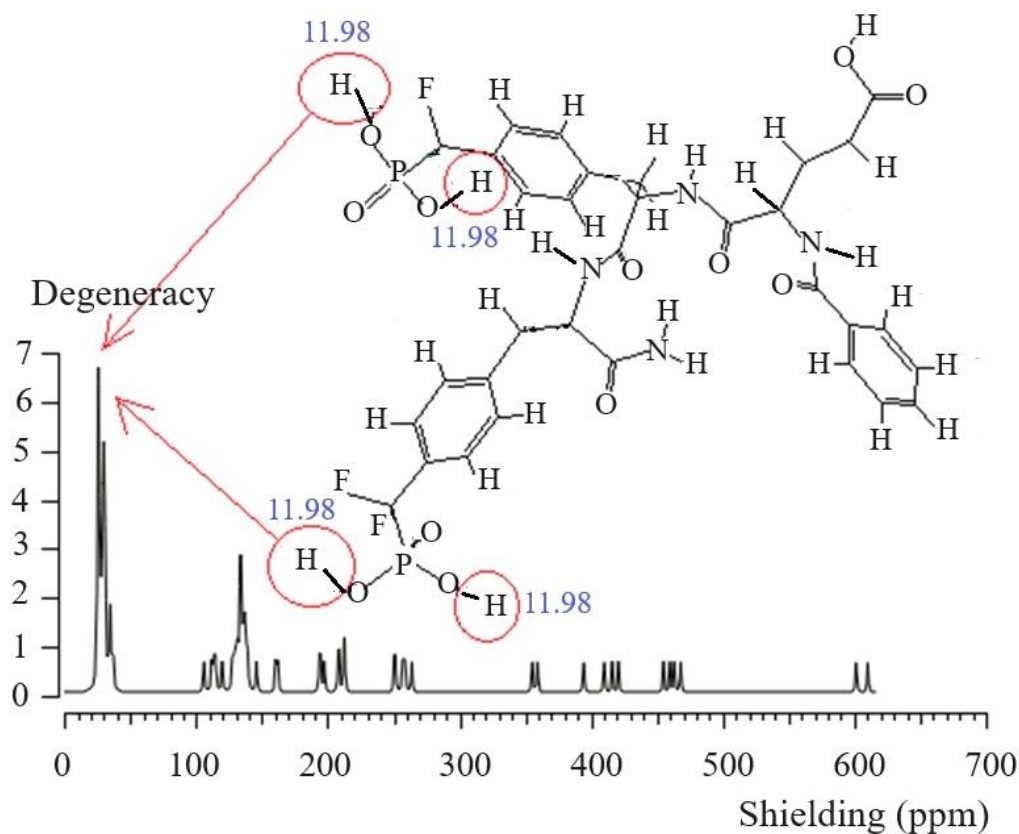
Figure 2 ^{1}H-NMR shielding of BzN-EJJ-amide adsorbed on the (5, 5) armchair SWCNT using SCF GIAO method due to B3LYP function and 6-311+G (2d, p) basis set basis set.

In fact, BzN-EJJ-amide has shown NMR shielding between 10-600 ppm with a sharp peak of 25 ppm and several weak peaks between 100-450 ppm (Figure 2). The hydrogens involved in the O-H of PO3 groups have been exhibited in the high degeneracy of NMR chemical shielding tensors (Figure 2).

In the next step, the atomic charge of functionalized atoms of N, P, O, and F in the attachment of BzN-EJJ-amide with (5, 5) armchair SWCNT was evaluated (Table 1).

The results of Table 1 in a polar area have indicated the potency of BzN-EJJ-amide as an anti-diabetic drug modeled using the drug delivery method. The most significant fluctuation in atomic charge has been seen for the oxygen atoms in O-H of PO3 groups as the electronegative atoms in the formation of the potent chelation with (5, 5) armchair carbon nanotube using the drug delivery approach, which has recommended the modelling of BzN-EJJ-amide → (5, 5) armchair SWCNT (Figure 3).
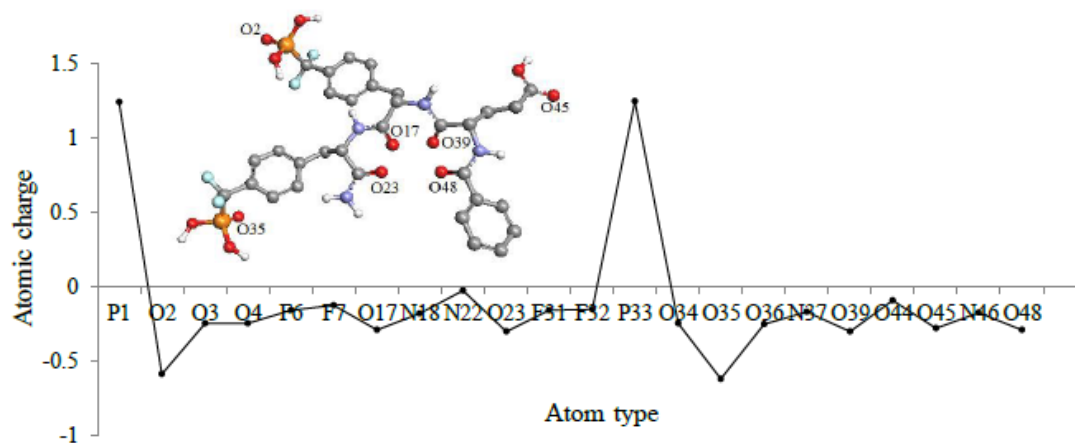
Figure 3 Changes of atomic charge for some electronegative atoms of N, P, O, and F in the active sites of BzN-EJJ-amide in the junction with (5, 5) armchair SWCNT.

This research recommends that the solid-state structure of the CNT in drug delivery can influence its properties, manufacturability, and stability. It is essential to regulate and control solid-state structure and subsequent properties. This work shows that NMR is closely related to the widely used technique of solution-state NMR and possesses many of the same features. Further, the study concludes that the pharmaceutical NMR field continues to develop quickly and will improve new molecular structures in delivery approaches.

Figure 3 shows the position of specific N, P, O, and F atoms in the active site of BzN-EJJ-amide → (5, 5) armchair SWCNT complex through the transferring charge of electrons from BzN-EJJ-amide towards (5, 5) SWCNT. The spin density and partial charges have been gained by matching the electrostatic potential to fix the charge of N, P, O, and F atoms with high electronegativity in the attachment of the electrophilic group of C in the structure of (5, 5) SWCNT sensor leads us toward the industry of drug delivery. The surface charge indicates possible electrostatic interactions between the CNT nanocarrier units, affects their aggregation tendencies, and helps select the proper drugs. It can be determined by applying an electrical current through the important labels of C30, F31, F32, P33, O34, O35, and O36 in the active site of CNT.

3.2 NQR Analysis

The electric potential of nuclear quadrupole resonance (NQR) (Table 1) was reported for the BP agent of BzN-EJJ-amide → (5, 5) armchair SWCNT complex using CAM-B3LYP/EPR-III, 6-311+G (2d,p) basis sets (Figure 4).
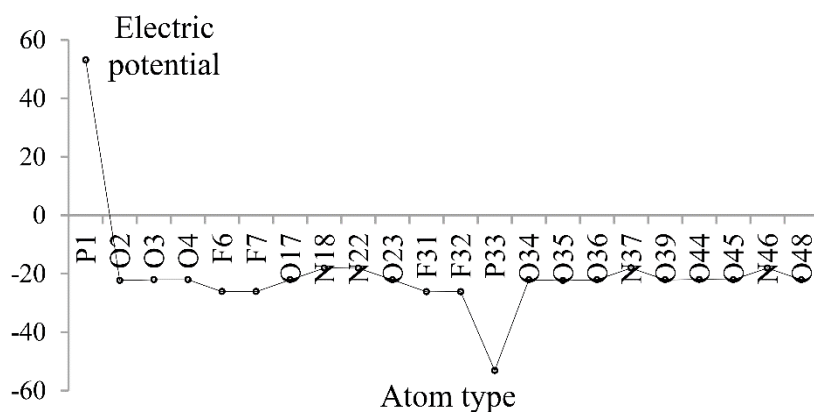
Figure 4 Alteration of the electric potential versus atom type through NQR calculation for BP agent of BzN-EJJ-amide in the water medium attached to the (5, 5) armchair SWCNT sensor.

The NQR method shortens detection times, eliminates spurious signals, and enhances the sensitivity of detection of ^{14}N frequencies through important labels of C30, F31, F32, P33, O34, O35, and O36 (Figure 4) with a sharp peak fluctuation around -53.14 a.u. of electric potential for P33 label.

3.3 Analysis of NBO

The Natural Bond Orbital (NBO) analysis of BzN-EJJ-amide as an anti-diabetes has demonstrated the character of electronic conjugation between bonds in the inhibitor and (5, 5) armchair SWCNT sensor (Table 2 & Figure 5).

Table 2 NBO analysis for BzN-EJJ-amide as an anti-diabetes drug adsorbed on the (5, 5) armchair SWCNT.

| Bond orbital	Occupancy	Hybrids
BD (1) P1 – O2	1.9746	0.6990 (sp$^{2.12}$) P + 0.7152 (sp$^{7.89}$) O
BD (1) P1 – O3	1.9720	0.6033 (sp$^{3.28}$) P + 0.7975 (sp$^{5.71}$) O
BD (1) P1 – O4	1.9731	0.6046 (sp$^{3.19}$) P + 0.7965 (sp$^{5.78}$) O
BD (1) P1 – C5	1.9347	0.6686 (sp$^{3.83}$) P + 0.7436 (sp$^{3.44}$) C
BD (1) O3 – H55	1.9860	0.7817 (sp$^{4.28}$) O + 0.6236 (σ) H
BD (1) O4 – H56	1.9865	0.7808 (sp$^{4.27}$) O + 0.6248 (σ) H
BD (1) C5 – F6	1.9877	0.6167 (sp$^{3.22}$) C + 0.7872 (sp$^{7.14}$) F
BD (1) C5 – F7	1.9881	0.6268 (sp$^{2.94}$) C + 0.7792 (sp$^{7.45}$) F
BD (1) C15 – N37	1.9790	0.6456 (sp$^{3.25}$) C + 0.7637 (sp$^{2.11}$) N
BD (1) C16 – O17	1.9930	0.6563 (sp$^{1.86}$) C + 0.7545 (sp$^{3.42}$) O
BD (1) C16 – N18	1.9865	0.6446 (sp$^{2.13}$) C + 0.7645 (sp$^{1.83}$) N
BD (1) N18 – C19	1.9783	0.7691 (sp$^{2.13}$) N + 0.6391 (sp$^{3.28}$) C
BD (1) C21 – N22	1.9903	0.6446 (sp$^{2.11}$) C + 0.7646 (sp$^{1.88}$) N
BD (1) C21 – O23	1.9935	0.6538 (sp$^{1.92}$) C + 0.7567 (sp$^{3.32}$) O
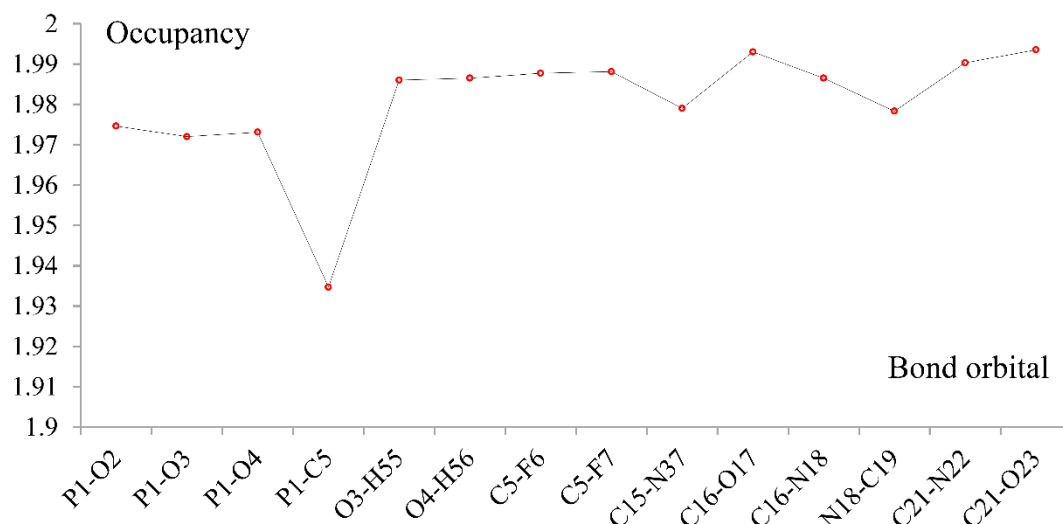
Figure 5 Occupancy fluctuation extracted from NBO method for BzN-EJJ-amide inhibitor adsorbed on the (5, 5) armchair SWCNT.

The fluctuation of occupancy of natural bond orbitals for BzN-EJJ-amide inhibitor adsorbed on the (5, 5) armchair SWCNT has been shown through bond orbitals containing P-O, O-H, C-F, C-N, C-O toward the Langmuir adsorption process by indicating the charge density from a heterocyclic compound of bisphosphonate agent close to the nanotube (Figure 5).

3.4 Electrostatic Potential (ESP) Map

Understanding the chemical reactivity and the atomic structure of molecules and solids needs the electrostatic potential (ESP), which represents some parameters such as A variety of properties, atomic and anionic radii, electronegativity, and energies [76].

The ESP is applied to explore electrophilic and nucleophilic sides, characterize hydrogen bonds, and analyze intermolecular interactions for single molecules or finite clusters of atoms (Figure 6) [77-79].
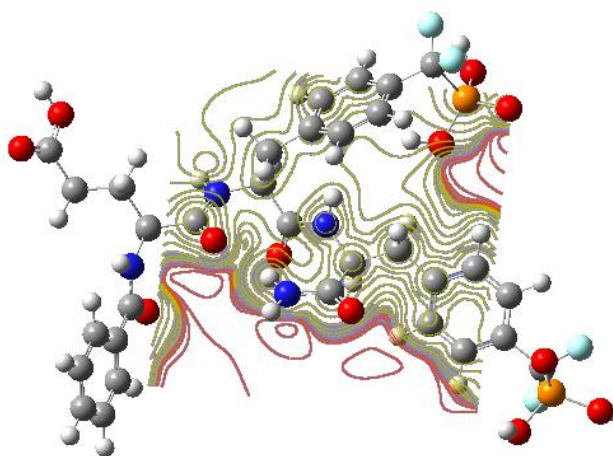

Figure 6 The ESP map for BP agent of BzN-EJJ-amide in the aqueous medium.

3.5 IR Spectroscopy

Based on Figure 7, the IR spectrum analysis, the authors have concluded that this protective film consisted of an [BzN-EJJ-amide → SWCNT] complex.
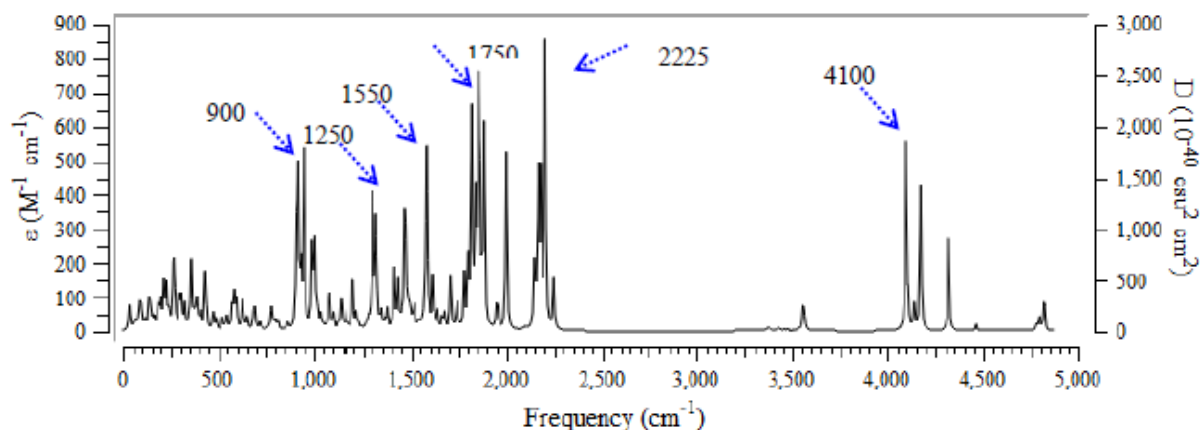

Figure 7 Diagram of IR spectra for BzN-EJJ-amid attached to the (5, 5) armchair SWCNT using CAM-B3LYP/6-311+G (2d,p) calculations.

The maximum IR spectrum has been seen in the frequency range between 250 cm^{-1}-4500 cm^{-1} by the most substantial peaks about 4100 cm^{-1}, 2250 cm^{-1}, 1750 cm^{-1}, 1550 cm^{-1}, 1250 cm^{-1}, and 900 cm^{-1}, respectively, for [BzN-EJJ-amide → SWCNT] (Figure 7).

3.6 Frontier Orbitals of HOMO & LUMO & UV-VIS Spectroscopy

The highest occupied molecular orbital energy (HOMO) and the lowest unoccupied molecular orbital energy (LUMO) have been calculated for the BP agent of BzN-EJJ-amide adsorbed onto (5, 5) armchair SWCNT sensor [80-83].

The HOMO, LUMO, and band energy gap (eV) have exhibited the pictorial description of the frontier molecular orbital's that is a significant key for knowing the molecular specifications of the drug delivery approach through attaching the BP agent of BzN-EJJ-amide which has been surrounded by H_2O molecules on the (5, 5) armchair SWCNT in aqueous medium (Scheme 3).

$E_{HOMO} = -0.2330$ a.u.

$\Delta E = 12.0186$ eV

$E_{LUMO} = 0.2086$ a.u.
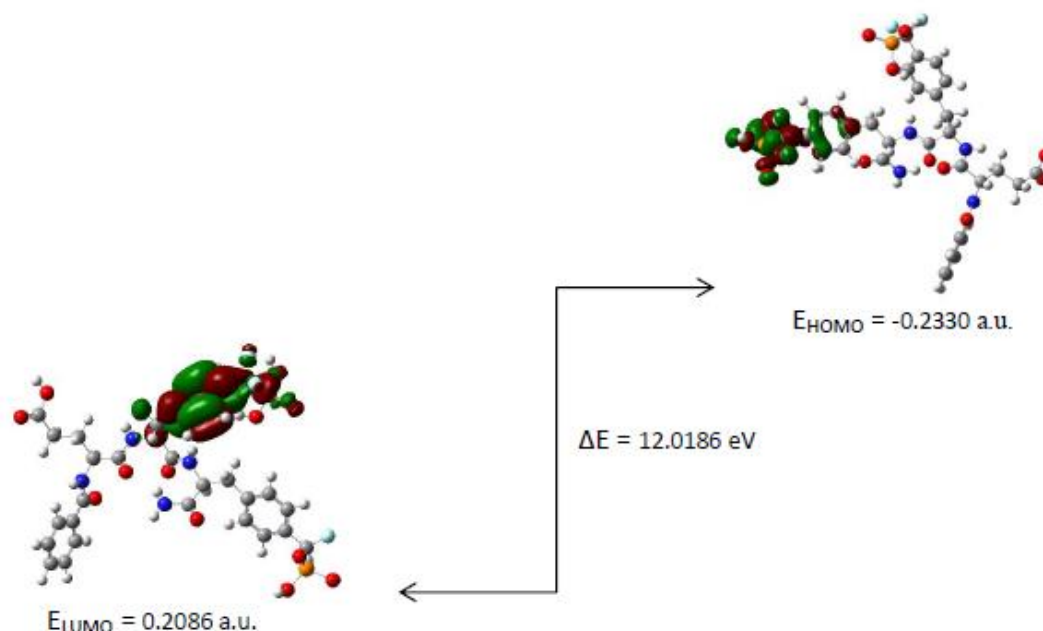
Scheme 3 The energy gap of HOMO/LUMO (a.u.) and band energy gap (ΔE/eV) for adsorbing BzN-EJJ-amide onto (5, 5) armchair SWCNT in aqueous medium.

The parameters in Table 3 exhibit good stability of the BP agent through Langmuir adsorption on the (5, 5) armchair SWCNT sensor. In this verdict, TD-DFT/6-311+G (2d,p) computations have been done to identify the low-lying excited states of BzN-EJJ-amide adsorbed on the (5, 5) armchair SWCNT. The results consist of the vertical excitation energies, oscillator strength and wavelength which have been introduced in Figure 8.

Table 3 The HOMO (a.u.), LUMO (a.u.), band energy gap (ΔE/ev), and other quantities (ev) for [BzN-EJJ-amide → SWCNT] in water medium.

Spin	HOMO	LUMO	ΔE	μ	χ	η
Singlet	-0.2330	0.2086	12.0186	-0.3311	0.3311	6.0093
Triplet	-0.2432	-0.2330	0.2778	-6.4794	6.4794	0.1389
Quintet	-0.2446	-0.2432	0.0392	-6.6379	6.6379	0.0196
Septet	-0.2602	-0.2446	0.4226	-6.8688	6.8688	0.2113
Nonet	-0.2792	-0.2602	0.5192	-7.3397	7.3397	0.2596
11-et	-0.2812	-0.2792	0.0533	-7.6259	7.6259	0.0266
13-et	-0.2837	-0.2812	0.0672	-7.6862	7.6862	0.0336
15-et	-0.2940	-0.2837	0.2802	-7.8600	7.8600	0.1401
17-et	-0.2999	-0.2940	0.1611	-8.0806	8.0806	0.0805
10-et	-0.3055	-0.2992	0.1700	-8.2280	8.2280	0.0850

$\Delta E = E_{LUMO} - E_{HOMO}$; $\mu = (E_{HOMO} + E_{LUMO})/2$; $\chi = -(E_{HOMO} + E_{LUMO})/2$; $\eta = (E_{LUMO} - E_{HOMO})/2$
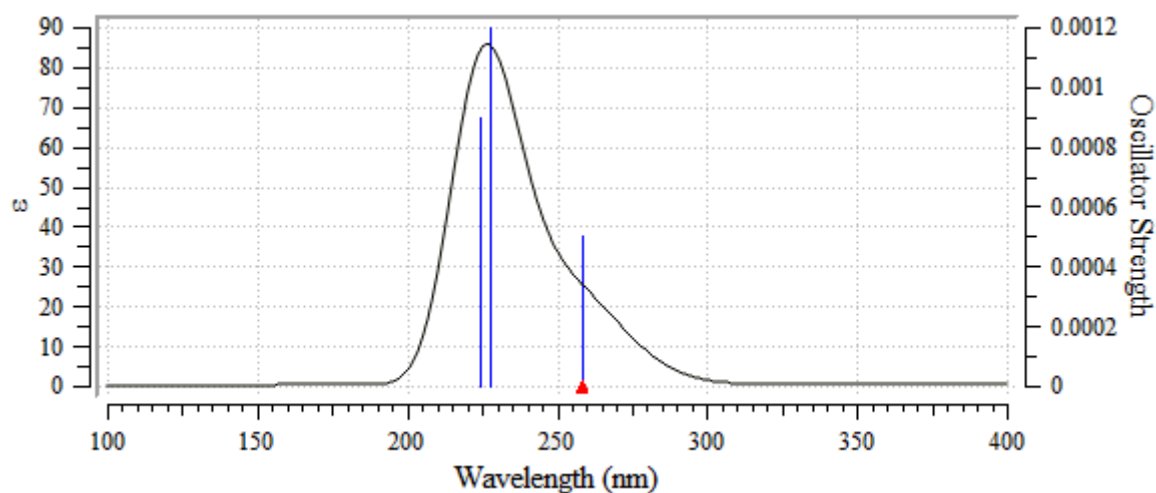
Figure 8 BzN-EJJ-amide is adsorbed on the (5, 5) armchair SWCNT.

Based on the computed amounts of UV-VIS spectrum for BzN-EJJ-amide adsorbed on the (5, 5) armchair SWCNT, there are maximum adsorption bands between 200 nm-275 nm, and maximum adsorption band has observed around 225 nm, 300 nm, and 240 nm, respectively (Figure 8). Using the quantum theory of atoms in molecules (QTAIMs) method, intermolecular interactions and corresponding parameters at critical bonding points were also investigated [84, 85].

4. Conclusions

According to this research, the outlook of NMR spectroscopy has indicated the position of active sites of labeled N, P, O, and F in the anti-diabetic drug of BzN-EJJ-amide attached to (5, 5) armchair SWCNT sensor, which transfers the electron density in polar bisphosphonate in the water medium toward (5, 5) armchair carbon nanotube. Moreover, NQR characteristics for BzN-EJJ-amide → (5, 5) armchair SWCNT complex have represented the most fluctuation in the zone of two phosphorus of PO_3 groups. The maximum IR spectrum for BzN-EJJ-amide → (5, 5) armchair SWCNT has been seen in the frequency range between 250 cm^{-1}-4500 cm^{-1} by the most substantial peaks about 4100 cm^{-1}, 2250 cm^{-1}, 1750 cm^{-1}, 1550 cm^{-1}, 1250 cm^{-1}, and 900 cm^{-1}, respectively. Furthermore, the energy gap has indicated the energy difference between frontier HOMO and LUMO orbital, introducing the stability for BzN-EJJ-amide and discovering the chemical potential of BzN-EJJ-amide drug for treatment type 2 diabetes.

Acknowledgments

Author Contributions

Fatemeh Mollaamin: Conceptualization and idea, Methodology, Software, Validation, Formal analysis, Investigation, Data Curation, Writing-original draft preparation, Visualization, Supervision, Project administration. Majid Monajjemi: Methodology, Software, Validation, Formal analysis, Investigation, Data Curation, Writing-review and editing, Visualization, Resources. Ahmad R.

Alsayed: Methodology, Validation, Formal analysis, Investigation, Data Curation, Writing-review and editing, Visualization, Resources.

Funding

Competing Interests

The authors declare that no competing interests exist.

References

1. Meigs JB, Muller DC, Nathan DM, Blake DR, Andres R. The natural history of progression from normal glucose tolerance to type 2 diabetes in the Baltimore Longitudinal Study of Aging. Diabetes. 2003; 52: 1475-1484.
2. Cosentino F, Grant PJ, Aboyans V, Bailey CJ, Ceriello A, Delgado V, et al. 2019 ESC Guidelines on diabetes, pre-diabetes, and cardiovascular diseases developed in collaboration with the EASD: The Task Force for diabetes, pre-diabetes, and cardiovascular diseases of the European Society of Cardiology (ESC) and the European Association for the Study of Diabetes (EASD). Eur Heart J. 2020; 41: 255-323.
3. Buse JB, Wexler DJ, Tsapas A, Rossing P, Mingrone G, Mathieu C, et al. 2019 update to: Management of hyperglycaemia in type 2 diabetes, 2018. A consensus report by the American Diabetes Association (ADA) and the European Association for the Study of Diabetes (EASD). Diabetologia. 2020; 63: 221-228.
4. Schnurr TM, Jakupović H, Carrasquilla GD, Ängquist L, Grarup N, Sørensen TI, et al. Obesity, unfavourable lifestyle and genetic risk of type 2 diabetes: A case-cohort study. Diabetologia. 2020; 63: 1324-1332.
5. Carlsson LM, Peltonen M, Ahlin S, Anveden Å, Bouchard C, Carlsson B, et al. Bariatric surgery and prevention of type 2 diabetes in Swedish obese subjects. N Engl J Med. 2012; 367: 695-704.
6. Asante-Appiah E, Patel S, Dufresne C, Roy P, Wang Q, Patel V, et al. The structure of PTP-1B in complex with a peptide inhibitor reveals an alternative binding mode for bisphosphonates. Biochemistry. 2002; 41: 9043-9051.
7. Dufresne C, Roy P, Wang Z, Asante-Appiah E, Cromlish W, Boie Y, et al. The development of potent non-peptidic PTP-1B inhibitors. Bioorg Med Chem Lett. 2004; 14: 1039-1042
8. Murthy VS, Kulkarni VM. Molecular modeling of protein tyrosine phosphatase 1B (PTP 1B) inhibitors. Bioorg Med Chem. 2002; 10: 897-906.
9. Genovese M, Imperatore C, Casertano M, Aiello A, Balestri F, Piazza L, et al. Dual targeting of PTP1B and aldose reductase with marine drug phosphoeleganin: A promising strategy for treatment of type 2 diabetes. Mar Drugs. 2021; 19: 535.
10. Mohsin SM, Hussein MZ, Sarijo SH, Fakurazi S, Arulselvan P, Taufiq-Yap YH. Characterisation and cytotoxicity assessment of UV absorbers-intercalated zinc/aluminium-layered double hydroxides on dermal fibroblast cells. Sci Adv Mater. 2014; 6: 648-658.
11. Saifullah B, Hussein MZ, Hussein-Al-Ali SH, Arulselvan P, Fakurazi S. Antituberculosis nanodelivery system with controlled-release properties based on para-amino salicylate-zinc

aluminum-layered double-hydroxide nanocomposites. Drug Des Devel Ther. 2013; 7: 1365-1375.

12. Barahuie F, Hussein MZ, Hussein-Al-Ali SH, Arulselvan P, Fakurazi S, Zainal Z. Preparation and controlled-release studies of a protocatechuic acid-magnesium/aluminum-layered double hydroxide nanocomposite. Int J Nanomed. 2013; 8: 1975-1987.

13. Kura AU, Ali SH, Hussein MZ, Fakurazi S, Arulselvan P. Development of a controlled-release anti-parkinsonian nanodelivery system using levodopa as the active agent. Int J Nanomed. 2013; 8: 1103-1100.

14. Mohsin SM, Hussein MZ, Sarijo SH, Fakurazi S, Arulselvan P, Hin TY. Synthesis of (cinnamate-zinc layered hydroxide) intercalation compound for sunscreen application. Chem Cent J. 2013; 7: 26.

15. Mohsin SM, Hussein MZ, Sarijo SH, Fakurazi S, Arulselvan P, Taufiq-Yap YH. Optimization of UV absorptivity of layered double hydroxide by intercalating organic UV-absorbent molecules. J Biomed Nanotechnol. 2014; 10: 1490-1500.

16. Cao X, Deng W, Fu M, Zhu Y, Liu H, Wang L, et al. Seventy-two-hour release formulation of the poorly soluble drug silybin based on porous silica nanoparticles: *In vitro* release kinetics and in vitro/in vivo correlations in beagle dogs. Eur J Pharm Sci. 2013; 48: 64-71.

17. Ghaffarian R, Bhowmick T, Muro S. Transport of nanocarriers across gastrointestinal epithelial cells by a new transcellular route induced by targeting ICAM-1. J Control Release. 2012; 163: 25-33.

18. Zhang L, Xue H, Cao Z, Keefe A, Wang J, Jiang S. Multifunctional and degradable zwitterionic nanogels for targeted delivery, enhanced MR imaging, reduction-sensitive drug release, and renal clearance. Biomaterials. 2011; 32: 4604-4608.

19. Bethune DS, Kiang CH, De Vries MS, Gorman G, Savoy R, Vazquez J, et al. Cobalt-catalysed growth of carbon nanotubes with single-atomic-layer walls. Nature. 1993; 363: 605-607.

20. Iijima S, Ichihashi T. Single-shell carbon nanotubes of 1-nm diameter. Nature. 1993; 363: 603-605.

21. Dai H. Carbon nanotubes: Opportunities and challenges. Surf Sci. 2002; 500: 218-241.

22. Abi TG, Karmakar T, Taraphder S. Proton affinity of polar amino acid sidechain analogues anchored to the outer wall of single walled carbon nanotubes. Comput Theor Chem. 2013; 1010: 53-66.

23. Feng W, Ji P. Enzymes immobilized on carbon nanotubes. Biotechnol Adv. 2011; 29: 889-895.

24. Chen Q, Kaneko T, Hatakeyama R. Characterization of pulse-driven gas-liquid interfacial discharge plasmas and application to synthesis of gold nanoparticle-DNA encapsulated carbon nanotubes. Curr Appl Phys. 2011; 11: S63-S66.

25. Mollaamin F, Shahriari S, Monajjemi M. Monkeypox disease treatment by tecovirimat adsorbed onto single-walled carbon nanotube through drug delivery method. J Chil Chem Soc. 2023; 68: 5796-5801.

26. Khaleghian M, Zahmatkesh M, Mollaamin F, Monajjemi M. Investigation of solvent effects on armchair single-walled carbon nanotubes: A QM/MD study. Fuller Nanotub Carbon Nanostructures. 2011; 19: 251-261.

27. Monajjemi M, Khaleghian M, Tadayonpour N, Mollaamin F. The effect of different solvents and temperatures on stability of single-walled carbon nanotube: A QM/MD study. Int J Nanosci. 2010; 9: 517-529.

28. Mollaamin F, Monajjemi M, Salemi S, Baei MT. A dielectric effect on normal mode analysis and symmetry of BNNT nanotube. Fuller Nanotub Carbon Nanostructures. 2011; 19: 182-196.

29. Khalili Hadad B, Mollaamin F, Monajjemi M. Biophysical chemistry of macrocycles for drug delivery: A theoretical study. Russ Chem Bull. 2011; 60: 238-241.

30. Sapino S, Chindamo G, Chirio D, Manzoli M, Peira E, Riganti C, et al. Calcium phosphate-coated lipid nanoparticles as a potential tool in bone diseases therapy. Nanomaterials. 2021; 11: 2983.

31. Park J, Cimpean A, Tesler AB, Mazare A. Anodic TiO$_2$ nanotubes: Tailoring osteoinduction via drug delivery. Nanomaterials. 2021; 11: 2359.

32. Gao L, Zhang SQ. Antiosteoporosis effects, pharmacokinetics, and drug delivery systems of icaritin: Advances and prospects. Pharmaceuticals. 2022; 15: 397.

33. Chindamo G, Sapino S, Peira E, Chirio D, Gonzalez MC, Gallarate M. Bone diseases: Current approach and future perspectives in drug delivery systems for bone targeted therapeutics. Nanomaterials. 2020; 10: 875.

34. Salamanna F, Gambardella A, Contartese D, Visani A, Fini M. Nano-based biomaterials as drug delivery systems against osteoporosis: A systematic review of preclinical and clinical evidence. Nanomaterials. 2021; 11: 530.

35. Choi S, Jo HS, Song H, Kim HJ, Oh JK, Cho JW, et al. Multifunctional tannic acid-alendronate nanocomplexes with antioxidant, anti-inflammatory, and osteogenic potency. Nanomaterials. 2021; 11: 1812.

36. Mollaamin F, Monajjemi M. Harmonic linear combination and normal mode analysis of semiconductor nanotubes vibrations. J Comput Theor Nanosci. 2015; 12: 1030-1039.

37. Mollaamin F. Computational methods in the drug delivery of carbon nanocarriers onto several compounds in Sarraceniaceae medicinal plant as monkeypox therapy. Computation. 2023; 11: 84.

38. Mollaamin F, Shahriari S, Monajjemi M. Treating omicron BA.4 & BA.5 via herbal antioxidant asafoetida: A DFT study of carbon nanocarrier in drug delivery. J Chil Chem Soc. 2023; 68: 5781-5786.

39. Sarasia EM, Afsharnezhad S, Honarparvar B, Mollaamin F, Monajjemi M. Theoretical study of solvent effect on NMR shielding tensors of luciferin derivatives. Phys Chem Fluids. 2011; 49: 561-571.

40. Monajjemi M, Mahdavian L, Mollaamin F, Khaleghian M. Interaction of Na, Mg, Al, Si with carbon nanotube (CNT): NMR and IR study. Russ J Inorg Chem. 2009; 54: 1465-1473.

41. Mollaamin F, Ilkhani A, Sakhaei N, Bonsakhteh B, Faridchehr A, Tohidi S, et al. Thermodynamic and solvent effect on dynamic structures of nano bilayer-cell membrane: Hydrogen bonding study. J Comput Theor Nanosci. 2015; 12: 3148-3154.

42. Mbese Z, Aderibigbe BA. Bisphosphonate-based conjugates and derivatives as potential therapeutic agents in osteoporosis, bone cancer and metastatic bone cancer. Int J Mol Sci. 2021; 22: 6869.

43. Rauner M, Taipaleenmäki H, Tsourdi E, Winter EM. Osteoporosis treatment with anti-sclerostin antibodies—Mechanisms of action and clinical application. J Clin Med. 2021; 10: 787.

44. Geiger I, Kammerlander C, Höfer C, Volland R, Trinemeier J, Henschelchen M, et al. Implementation of an integrated care programme to avoid fragility fractures of the hip in older adults in 18 Bavarian hospitals–study protocol for the cluster-randomised controlled fracture liaison service FLS-CARE. BMC Geriatr. 2021; 21: 43.

45. Hayes KN, He N, Brown KA, Cheung AM, Juurlink DN, Cadarette SM. Over half of seniors who start oral bisphosphonate therapy are exposed for 3 or more years: Novel rolling window approach and patterns of use. Osteoporos Int. 2021; 32: 1413-1420.

46. Sølling AS, Christensen DH, Darvalics B, Harsløf T, Thomsen RW, Langdahl B. Fracture rates in patients discontinuing alendronate treatment in real life: A population-based cohort study. Osteoporos Int. 2021; 32: 1103-1115.

47. Kim JW, Yee J, Oh SH, Kim SH, Kim SJ, Chung JE, et al. Machine learning approaches for predicting bisphosphonate-related osteonecrosis in women with osteoporosis using VEGFA gene polymorphisms. J Pers Med. 2021; 11: 541.

48. Langdahl BL. Overview of treatment approaches to osteoporosis. Br J Pharmacol. 2021; 178: 1891-1906.

49. Mollaamin F & Monajjemi M. Application of DFT/TD-DFT Frameworks in the Drug Delivery Mechanism: Investigation of Chelated Bisphosphonate with Transition Metal Cations in Bone Treatment. Chemistry. 2023; 5: 365-380.

50. Thompson K, Rogers MJ. The molecular mechanisms of action of bisphosphonates. Clin Rev Bone Miner Metab. 2007; 5: 130-144.

51. Russell RG, Watts NB, Ebetino FH, Rogers MJ. Mechanisms of action of bisphosphonates: Similarities and differences and their potential influence on clinical efficacy. Osteoporos Int. 2008; 19: 733-759.

52. Mollaamin F & Monajjemi M. Carbon Nanotubes as Biosensors for Releasing Conjugated Bisphosphonates–Metal Ions in Bone Tissue: Targeted Drug Delivery through the DFT Method. C — Journal of Carbon Research. 2023; 9: 61.

53. Mollaamin F & Monajjemi M. Determination of SWCNT biosensor for bisphosphonate–2X(X = Mg^{2+}, Ca^{2+}, Sr^{2+}) delivery in bone cell through electromagnetic and thermodynamic analysis using QM/MC methods. Sensor Review. 2024, 44: 100-112.

54. Liu GX, Tan JZ, Niu CY, Shen JH, Luo XM, shen X, et al. Molecular dynamics simulations of interaction between protein-tyrosine phosphatase 1B and a bidentate inhibitor[1]. Acta Pharmacol Sin. 2006; 27: 100-110.

55. Mollaamin F. Conocimiento de enfermedades virales terapéuticas: Aplicación de SWCNT en la administración de fármacos. Rev Colomb Quimica. 2023; 52: 28-35.

56. Mollaamin F. Structural and functional characterization of medicinal plants as selective antibodies towards therapy of COVID-19 symptoms. Antibodies. 2024; 13: 38.

57. Hohenberg P, Kohn W. Inhomogeneous electron gas. Phys Rev. 1964; 136: B864-B871.

58. Monajjemi M, Mollaamin F, Shojaei S. An overview on Coronaviruses family from past to COVID-19: Introduce some inhibitors as antiviruses from Gillan's plants. Biointerface Res Appl Chem. 2020; 10: 5575-5585.

59. Zadeh MA, Lari H, Kharghanian L, Balali E, Khadivi R, Yahyaei H, et al. Density functional theory study and anti-cancer properties of shyshaq plant: In view point of nano biotechnology. J Comput Theor Nanosci. 2015; 12: 4358-4367.

60. Monajjemi M, Shahriari S, Mollaamin F. Evaluation of coronavirus families & COVID-19 proteins: Molecular modeling study. Biointerface Res Appl Chem. 2020; 10: 6039-6057.

61. Cramer CJ, Truhlar DG. PM3-SM3: A general parameterization for including aqueous solvation effects in the PM3 molecular orbital model. J Computat Chem. 1992; 13: 1089-1097.

62. Mollaamin F, Shahriari S, Monajjemi M. Drug design of medicinal plants as a treatment of Omicron variant (COVID-19 VARIANT B.1.1.529). J Chil Chem Soc. 2022; 67: 5562-5570.

63. Chambers CC, Hawkins GD, Cramer CJ, Truhlar DG. Model for aqueous solvation based on class IV atomic charges and first solvation shell effects. J Phys Chem. 1996; 100: 16385-16398.

64. Shahriari S, Monajjemi M, Mollaamin F. Determination of proteins specification with SARS-COVID-19 based ligand designing. J Chil Chem Soc. 2022; 67: 5468-5476.

65. Onsager L. Electric moments of molecules in liquids. J Am Chem Soc. 1936; 58: 1486-1493.

66. Tomasi J. Cavity and reaction field: "Robust" concepts. Perspective on "Electric moments of molecules in liquids". Theor Chem Acc. 2000; 103: 196-199.

67. Rauch L, Hein R, Biedermann T, Eyerich K, Lauffer F. Bisphosphonates for the treatment of calcinosis cutis-A retrospective single-center study. Biomedicines. 2021; 9: 1698.

68. Mollaamin F, Monajjemi M. Adsorption ability of Ga5N10 nanomaterial for removing metal ions contamination from drinking water by DFT. Int J Quantum Chem. 2024; 124: e27348.

69. Smith JA. Nuclear quadrupole resonance spectroscopy. J Chem Educ. 1971; 48: 39-41.

70. Garroway AN, Naval Research Laboratory. Appendix K: Nuclear quadrupole resonance. In: Alternatives for Landmine Detection. Santa Monica, CA: Rand Corporation; 2003; MR-1608.

71. Poleshchuk OK, Kalinina EL, Latosińska JN, Koput J. Application of density functional theory to the analysis of electronic structure and quadrupole interaction in dimers of transition and non-transition elements. J Mol Struct. 2001; 574: 233-243.

72. Young HA, Freedman RD. Sears and Zemansky's University Physics with Modern Physics. 13th ed. Boston, MA: Addison-Wesley; 2012. 754p.

73. Coppens P. X-Ray Charge Densities and Chemical Bonding. Oxford: Oxford University Press; 1997.

74. Becker P, Coppens P. About the Coulomb potential in crystals. Acta Crystallogr A. 1990; 46: 254-258.

75. Frisch MJ, Trucks GW, Schlegel HB, Scuseria GE, Robb MA, Cheeseman JR, et al. Gaussian 16, Revision C.01. Wallingford, CT: Gaussian, Inc.; 2016.

76. Politzer P, Murray JS. The fundamental nature and role of the electrostatic potential in atoms and molecules. Theor Chem Acc. 2002; 108: 134-142.

77. Kumar A, Yeole SD, Gadre SR, López R, Rico JF, Ramírez G, et al. DAMQT 2.1.0: A new version of the DAMQT package enabled with the topographical analysis of electron density and electrostatic potential in molecules. J Comput Chem. 2015; 36: 2350-2359.

78. Niranjana Devi R, Jelsch C, Israel S, Aubert E, Anzline C, Hosamani AA. Charge density analysis of metformin chloride, a biguanide anti-hyperglycemic agent. Acta Crystallogr B. 2017; 73: 10-22.

79. Zhurova EA, Zhurov VV, Kumaradhas P, Cenedese S, Pinkerton AA. Charge density and electrostatic potential study of 16α, 17β-estriol and the binding of estrogen molecules to the estrogen receptors ERα and ERβ. J Phys Chem B. 2016; 120: 8882-8891.

80. Aihara JI. Reduced HOMO−LUMO gap as an index of kinetic stability for polycyclic aromatic hydrocarbons. J Phys Chem A. 1999; 103: 7487-7495.

81. Parr RG, Pearson RG. Absolute hardness: Companion parameter to absolute electronegativity. J Am Chem Soc. 1983; 105: 7512-7516.

82. Politzer P, Abu-Awwad F. A comparative analysis of Hartree-Fock and Kohn-Sham orbital energies. Theor Chem Acc. 1998; 99: 83-87.

83. Bakhshi K, Mollaamin F, Monajjemi AM. Exchange and correlation effect of hydrogen chemisorption on nano V (100) surface: A DFT study by generalized gradient approximation (GGA). J Comput Theor Nanosci. 2011; 8: 763-768.

84. Monajjemi M, Baie MT, Mollaamin AF. Interaction between threonine and cadmium cation in [Cd (Thr)$_n$]$^{2+}$ (*n* = 1–3) complexes: Density functional calculations. Russ Chem Bull. 2010; 59: 886-889.

85. Tahan A, Mollaamin F, Monajjemi AM. Thermochemistry and NBO analysis of peptide bond: Investigation of basis sets and binding energy. Russ J Phys Chem A. 2009; 83: 587-597.